MIT Open Access Articles

1H detection and dynamic nuclear polarization–enhanced NMR of A#1-42 fibrils

Massachusetts Institute of Technology

¹H detection and dynamic nuclear polarization–enhanced NMR of Aβ$_{1-42}$ fibrils

Salima Bahri[a], Robert Silvers[a,b], Brian Michael[a], Kristaps Jaudzems[c] (ORCID), Daniela Lalli[c], Gilles Casano[d], Olivier Ouari[d], Anne Lesage[c], Guido Pintacuda[c], Sara Linse[e] (ORCID), and Robert G. Griffin[a,1] (ORCID)

[a]Department of Chemistry and Francis Bitter Magnet Laboratory, Massachusetts Institute of Technology, Cambridge, MA 02139; [b]Department of Chemistry and Biochemistry, Institute of Molecular Biophysics, Florida State University, Tallahassee, FL 32306; [c]Centre de Résonance Magnétique Nucléaire (RMN) a Très Hauts Champs, CNRS/École Normale Supérieure Lyon/Claude Bernard University Lyon 1, Université de Lyon, Villeurbanne 69100, France; [d]Institut de Chimie Radicalaire, CNRS/Aix Marseille Université, Marseille 13013, France; and [e]Department of Chemistry, Lund University, Lund SE 22362, Sweden

Several publications describing high-resolution structures of amyloid-β (Aβ) and other fibrils have demonstrated that magic-angle spinning (MAS) NMR spectroscopy is an ideal tool for studying amyloids at atomic resolution. Nonetheless, MAS NMR suffers from low sensitivity, requiring relatively large amounts of samples and extensive signal acquisition periods, which in turn limits the questions that can be addressed by atomic-level spectroscopic studies. Here, we show that these drawbacks are removed by utilizing two relatively recent additions to the repertoire of MAS NMR experiments—namely, ¹H detection and dynamic nuclear polarization (DNP). We show resolved and sensitive two-dimensional (2D) and three-dimensional (3D) correlations obtained on ¹³C,¹⁵N-enriched, and fully protonated samples of M$_0$Aβ$_{1-42}$ fibrils by high-field ¹H-detected NMR at 23.4 T and 18.8 T, and ¹³C-detected DNP MAS NMR at 18.8 T. These spectra enable nearly complete resonance assignment of the core of M$_0$Aβ$_{1-42}$ (K16-A42) using submilligram sample quantities, as well as the detection of numerous unambiguous internuclear proximities defining both the structure of the core and the arrangement of the different monomers. An estimate of the sensitivity of the two approaches indicates that the DNP experiments are currently ~6.5 times more sensitive than ¹H detection. These results suggest that ¹H detection and DNP may be the spectroscopic approaches of choice for future studies of Aβ and other amyloid systems.

amyloid β$_{1-42}$ | magic-angle spinning | dynamic nuclear polarization | ¹H detection

Amyloid fibrils are highly stable protein deposits found in β-sheet conformations and are notoriously recognized as disruptive agents to cellular function in over 40 human diseases (1, 2). Alzheimer's disease (AD) is the most pervasive of all known plaque-related diseases and is associated with the presence of amyloid-β (Aβ) peptides in the extracellular space of the brain (3–6). As of 2021, there are ~6.2 million people in the United States living with Alzheimer's dementia and ~50 million worldwide (7), and there is as of yet no cure available for AD. In order to address this epidemic, it is essential that we learn as much as possible about the formation and structure of Aβ plaques, including the detailed features of their catalytic surface, in order to design and develop appropriate treatments to limit the propagation of aggregates and the generation of toxic forms.

Aβ is derived from the C-terminal region of the amyloid precursor protein (APP), a membrane protein in neuronal cells, via proteolysis by β- and γ-secretase (8, 9). One of the principal challenges in rationalizing AD etiology is Aβs diversity in peptide length, mutations, and posttranslational modifications (10). Their low solubility renders solution NMR ineffective, and high-resolution diffraction analyses have thus far been restricted to shorter peptides with all or most residues being ordered in the fibril core structure (11). Cryogenic electron microscopy (cryo-EM) has made strides in resolution in fibril studies within the past decade (12–18), but faces challenges studying with atomic-level detail due to polymorphism and heterogeneity in the fibril macroassemblies. Studying the individual and collective roles of amyloids at atomic resolution therefore requires alternative, high-resolution, high-throughput techniques for structural analysis. Magic-angle spinning NMR (MAS-NMR) was introduced as a technique with the potential to address these problems (19, 20). Recent technical advances (21, 22) and progress in sample preparation (23) have vastly improved the sensitivity and resolution of the spectra (24). Accordingly, there are now publications describing high-resolution structures of Aβ (25–29) and other amyloid (12, 16, 30–35) fibrils based on distance and torsion angle constraints derived from MAS experiments.

To date, all of the known NMR structures of amyloid fibrils were determined using constraints obtained from ¹³C/¹⁵N MAS spectra, which are inhomogeneously broadened and therefore feature well-resolved lines at low spinning frequencies (<25 kHz) (36). However, resolution often remains insufficient for in-depth analysis, and

Significance

Amyloid-β (Aβ) is the subject of intense scrutiny because of its close association with Alzheimer's disease (AD), which currently afflicts about 50 million people worldwide. The results reported in this manuscript focus on the new possibilities provided by ultrafast magic-angle spinning (MAS) ¹H detection and fast-MAS dynamic nuclear polarization (DNP), which have ushered in a new era for NMR-based structural biology, but whose potential has not yet been fully exploited for the structural investigation of complex amyloid assemblies. This work demonstrates the expeditious structural analysis of amyloid fibrils, without requiring preparation of large sample amounts, and sets the stage for future studies of unlabeled AD peptides derived from tissue samples available in limited quantities.

the experiments require relatively large amounts of peptide and extensive signal acquisition periods. Two relatively recent additions to the repertoire of MAS NMR experiments—namely, ^{1}H detection and dynamic nuclear polarization (DNP)—promise to circumvent these issues by reducing signal acquisition times or, alternatively, the amount of protein required for the experiment (37). ^{1}H detection offers a factor of $(\gamma_H/\gamma_S)^{3/2}$ gain in sensitivity, where S is usually a low γ-spin (38–40) such as ^{13}C or ^{15}N. In these two cases it is possible to achieve a factor of ~8 or ~32 gain in sensitivity, respectively. Importantly, ^{1}H detection also introduces an additional spectral dimension and therefore significantly increases the resolution. In parallel, DNP offers a general approach to enhancing sensitivity by factors of ~100, dramatically reducing signal acquisition times (by ~10^4). It does so by exploiting the high spin polarization of unpaired electrons (of gyromagnetic ratio γ_e ~660 times larger than γ_H) of a paramagnetic polarizing agent to enhance sensitivity by a theoretical factor of γ_e/γ_H. (41–44) Furthermore, DNP experiments are conducted at ~100 K, thereby increasing the Boltzmann polarization and sensitivity by another factor of ~3 over experiments conducted at ambient temperature (45).

While these arguments are well established for MAS NMR in many systems, it is less obvious that they are applicable to amyloid samples because spectra of amyloids are known to be broad for a variety of reasons, such as sample purity and polymorphism. Furthermore, ^{1}H-detected NMR at moderate MAS frequencies (~20 to 60 kHz) needs to be coupled to different levels of deuteration to ensure high sensitivity and narrow linewidths (42). Accordingly, deuteration with partial reprotonation of the amide or Hα sites has been implemented in pioneering studies on Aβ_{1-40} at 20 kHz MAS (46), HET-s(218–289) (47), and D76N-β2m at 60 kHz MAS (48). In addition, selective protonation in Aβ_{1-40} fibril methyl groups at 18 kHz MAS has led to highly resolved ^{1}H-detected ^{13}C correlations (49). In deuterated samples, however, the amount of potentially available structural information is significantly reduced, which can impair high-resolution structure determinations. The advent of 0.7 mm MAS rotors that achieve $\omega_r/2\pi$ >110 kHz attenuates ^{1}H-^{1}H dipole couplings and allows direct acquisition of multidimensional ^{1}H data without requiring deuteration (50). Furthermore, the spectra provide assignments and structural information. While a proof-of-concept application of this approach was demonstrated on fully protonated highly regular prion fibrils (51, 52), it is not clear whether this methodology is generally applicable and extendable to the detection of resolved inter- and intramolecular contacts in complex amyloid assemblies.

In parallel, our MAS DNP studies on M$_0$Aβ_{1-42} (28, 32, 53) report significant broadening of the NMR lines at cryogenic temperatures, which was attributed to distributions of conformations trapped at low temperature and is therefore inhomogeneous in origin. The loss of resolution associated with the MAS DNP methodology is a major obstacle for the detailed structural study of uniformly labeled amyloid samples. Concurrently, reports of well-resolved spectra at high fields and spinning frequencies suggest that the broadening is homogeneous (54–56). The advent of DNP instrumentation operating at high magnetic fields (18.8 T) and faster MAS ($\omega_r/2\pi$ = 40 kHz) provides an approach to alleviate this limitation by attenuating homogeneous couplings (57). However, this comes at the expense of the enhancement factor, potentially compromising the capacity to carry out expeditious multidimensional and multinuclear correlations. Moreover, NMR spectra of amyloid fibrils are known to suffer from additional debilitating broadening associated with their heterogeneous character (sample purity, polymorphism, etc.), which may mitigate the benefits of high magnetic fields.

In this work, we show that high resolution and sensitivity are possible for fibrils of M$_0$-Aβ_{1-42}. Notably, we demonstrate rapid resonance assignment and site-resolved detection of numerous site-specific internuclear proximities on submilligram sample
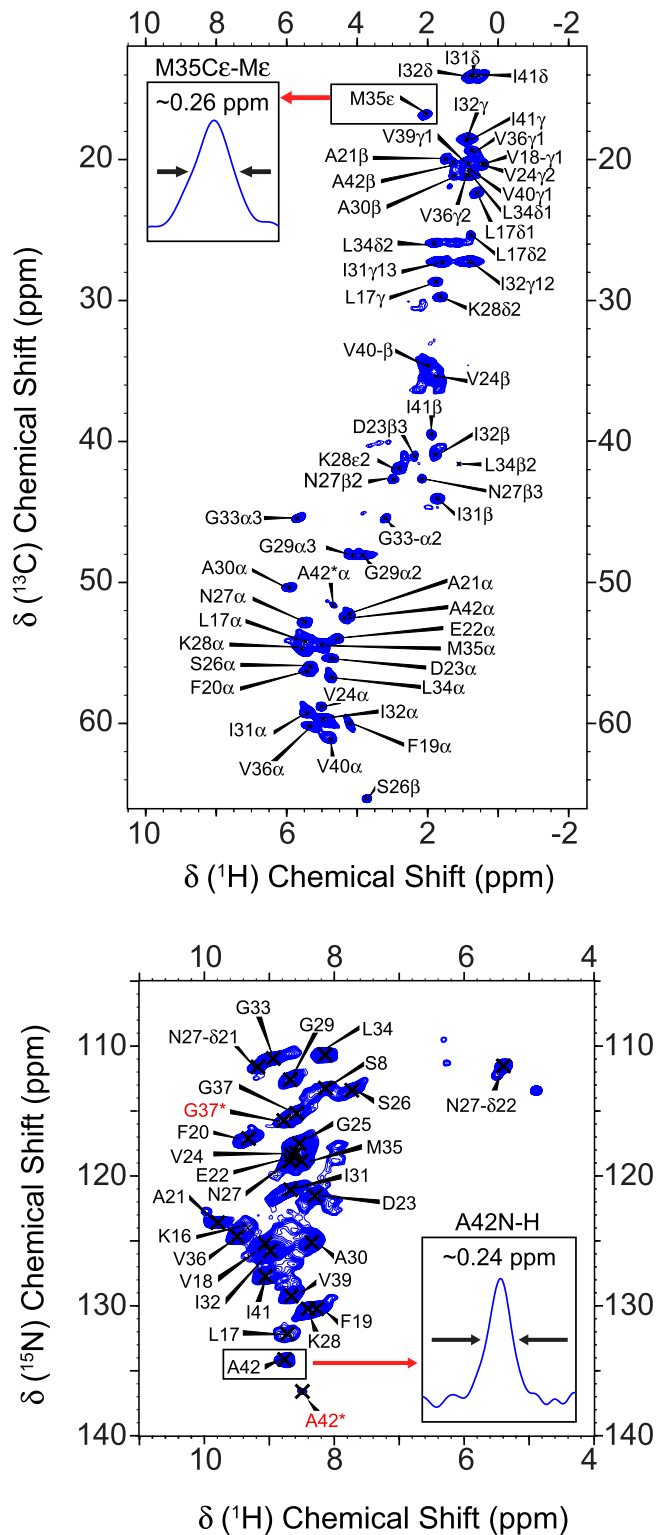
Fig. 1. High-resolution ^{1}H-detected spectra recorded on fully protonated U-^{13}C,^{15}N-labeled M$_0$-Aβ_{1-42} at 111.111 kHz MAS. (*Top*) 2D ^{13}C-^{1}H CP-HSQC; (*Bottom*) 2D ^{15}N-^{1}H CP-HSQC.

quantities via ^{1}H-detected NMR at $\omega_r/2\pi$ ~110 kHz and high field (23.4 T/1,000 MHz for ^{1}H) at room temperature and ^{13}C-detected DNP MAS NMR at $\omega_r/2\pi$ = 40 kHz and high field (18.8 T/800 MHz for ^{1}H) at low temperature. While both ^{1}H detection and DNP afford increased sensitivity, we estimate, using approaches outlined by Ishii and Tycko (40), that DNP, with our

current $\varepsilon = 22$, yields a factor of ~6.5 higher sensitivity. These results therefore illuminate possible paths for the rapid structure elucidation of amyloid fibrils available in limited quantities.

Results and Discussion

Under physiological conditions (pH ~7 to 8), M_0-$A\beta_{1-42}$ fibrils formed in vitro contain two filaments, and each filament is a C_2 symmetric dimer, in which K16-A42 forms the fibril core while D1-H14 is disordered and likely solvent exposed (28, 29, 35). Twelve residues of each monomer are buried in the hydrophobic core, while the fibril surface has a mixed hydrophobic, hydrophilic, and charged character with the A42 C-terminal carboxyl group and K28 sidechain forming a so-called salt bridge. Recently, Wickramasinghe et al. identified a new form of $A\beta_{1-42}$ using ${}^{1}H$ detection on brain-seeded fibrils (58). Likewise, a very different structure of $A\beta_{1-42}$ was published by Gremer et al. (15). However, these latter fibrils were grown at pH = 2 in 30% CH_3CN, which likely accounts for the disparity. We can thus say that M_0-$A\beta_{1-42}$ fibrils that have been formed under physiological conditions and without brain plaque seeding have a reproducible structure and are therefore a well-characterized system useful to develop novel techniques using MAS NMR.

${}^{1}H$-Detected Aβ Spectra. Fig. 1 shows two-dimensional (2D) ${}^{1}H,{}^{15}N$ and ${}^{1}H,{}^{13}C$ fingerprints of fully protonated U-${}^{13}C,{}^{15}N$-labeled M_0-$A\beta_{1-42}$ fibrils recorded at $\omega_r/2\pi = 110$ kHz on a 1-GHz spectrometer. These spectra represent dipolar-driven correlations that reveal interactions between nuclei that have little or no dynamics (59). Consequently, our existing ${}^{13}C/{}^{15}N$ assignments for M_0-$A\beta_{1-42}$ fibrils (24) led us to quickly identify many H^α and H^N resonances from the fibril core without the need for further correlations (60). These spectra feature both excellent resolution and sensitivity for all amide and aliphatic protons in the backbone and sidechains. Signals have linewidths of ~0.2 to 0.3 ppm, which are larger than those observed under similar conditions on microcrystalline proteins (50) but nonetheless guarantee a good dispersion and limited overlap. Most importantly, the resonances feature very long coherence lifetimes (e.g., bulk T_2s of ~70 and 40 ms were measured for ${}^{15}N$ and ${}^{13}C_\alpha$, respectively). This allows the acquisition of two three-dimensional (3D) experiments for sequential backbone assignment based on the detection of H^N protons, namely (H)CANH and (HCO)-CA-(CO)NH that correlate the intra- and interresidual CA to the H^N-N pair (60), as well as ${}^{1}H$-detected (H)NCAHA and ${}^{13}C$-${}^{13}C$ TOCSY-HSQC

correlations for sidechain resonance assignments (51). These spectra required only ~0.5 mg of sample and a few days of data acquisition to yield the complete identification of backbone and sidechain signals (~92% completeness) within the fibril core, consistent with the existing ${}^{13}C/{}^{15}N$ assignments for M_0-$A\beta_{1-42}$ fibrils (28).

At the same time, $\omega_r/2\pi = 110$ kHz MAS approaches the limit at which highly flexible regions appear in dipolar-based spectra. As a result, we observed that Gly37 and Ala42 exist in two distinct states, which are visible in the 2D CP-HSQC spectrum (in red in Fig. 1). These instances of polymorphism were not detectable in our previous experiments at 20 kHz MAS, suggesting that they derive from backbone flexibility in the C-terminal region. Likewise, several more resonances appear that have no apparent correlation to neighboring nuclei and likely arise from the N-terminal residues of the fibril or polymorphs of the fibril core (61).

Ultimately, ${}^{1}H$ detection has the potential to provide direct access to ${}^{1}H$-${}^{1}H$ distances for structure calculations, as shown in microcrystalline proteins (62), viral assemblies (50), and membrane-embedded proteins (63, 64). Here, we implemented radio frequency driven recoupling (RFDR) mixing into 3D HN and HC dipolar correlation schemes [(H)NHH or (H)CHH sequences], with representative slices from these datasets in Fig. 2A. Even with shorter mixing times, RFDR transfers polarization between protons that are further apart than typical one- or two-bond ${}^{13}C$-${}^{13}C$ distances that we typically achieve at moderate spinning frequencies. As a result, these spectra contain correlations between sequential or near-neighbor residues but also a number of unambiguous long-distance contacts up to 4 to 5 Å. These experiments can alternatively be performed as ${}^{13}C$-edited variants, to increase the spectral resolution through the indirect evolution of two carbon dimensions in the 3D ${}^{13}C$, ${}^{13}C$-edited ${}^{1}H$-${}^{1}H$ RFDR experiment (Fig. 2B). Although the additional pair of forward and backward H-C cross-polarization transfers causes a twofold drop in sensitivity, it allowed identification of a large number of unambiguous contacts listed in *SI Appendix*.

Overall, while faster spinning would still be required to make clear and quantitative interpretation of these ${}^{1}H$-${}^{1}H$ distance measurements, these contacts map the aliphatic sidechains within the hydrophobic "steric zipper," some of which are illustrated in Fig. 2C. One of the most important was to confirm the position of F19 and F20 on the inside of the β-strand as shown in Fig. 2C. This conformation was observed in the ${}^{13}C$-${}^{13}C$ spectra but is unusual, and an independent observation is important.
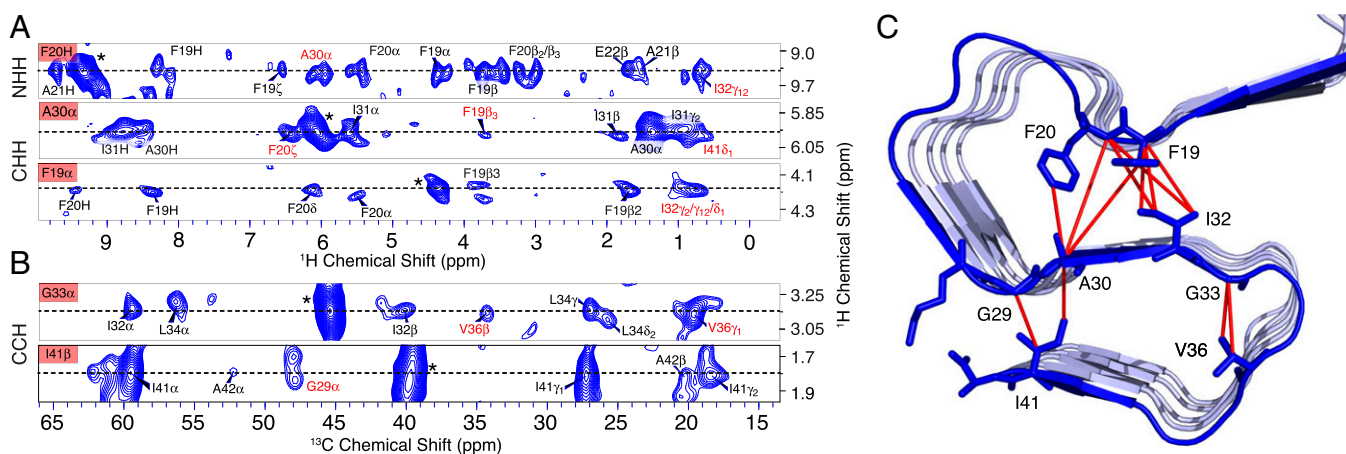
Fig. 2. Representative restraints from the (A) 3D (H)NHH, (H)CHH and (B) (H)C(HH)CH spectra that show long-range ${}^{1}H$-${}^{1}H$ contacts corresponding to the intramolecular structure of M_0-$A\beta_{1-42}$, highlighted in red. Asterisks mark diagonal peaks. (A) The NHH and CHH experiments establish contacts between F20H and I32γ_{12} and A30α, between A30α and F20ζ F19β_3 and I42δ_1, and from F19α to I32$\gamma_2/\gamma_{12}/\delta_1$. (B) The CCH experiments establish contacts between G33α and V36β and V36γ_1 and between I41β and G29α. (C) Display of intramolecular contacts found in the spectra shown in Fig. 3 on the lowest energy NMR structure of $M_0A\beta_{1-42}$ (Protein Data Bank ID 5kk3) (28). The contacts illustrated in this figure are listed in the legend for Fig. 3.

¹³C DNP Experiments. A full determination of fibril architecture additionally requires measuring intermolecular interactions among different monomers, and the 3D spectra described above contain additional cross-peaks between pairs of residues at the interface (e.g., H K16–Mε M35 Hα L17–Hγ L34 or H L17–Mε M35). However, the repetitive structure of the assembly does not allow assigning the experimental cross-peak intensity as intermolecular restraints in an unambiguous fashion. Current

protocols to address this problem rely on mixed samples obtained from differently isotopically labeled species (52, 65, 66). Such approaches have been successfully applied to describe interstrand arrangements and intermonomer contacts, but the necessary dilution of the labeled spins further reduces sensitivity and consequently requires even larger sample quantities. In these situations, MAS DNP at low temperature has a unique potential to complement ¹H-detected NMR studies at room temperature.
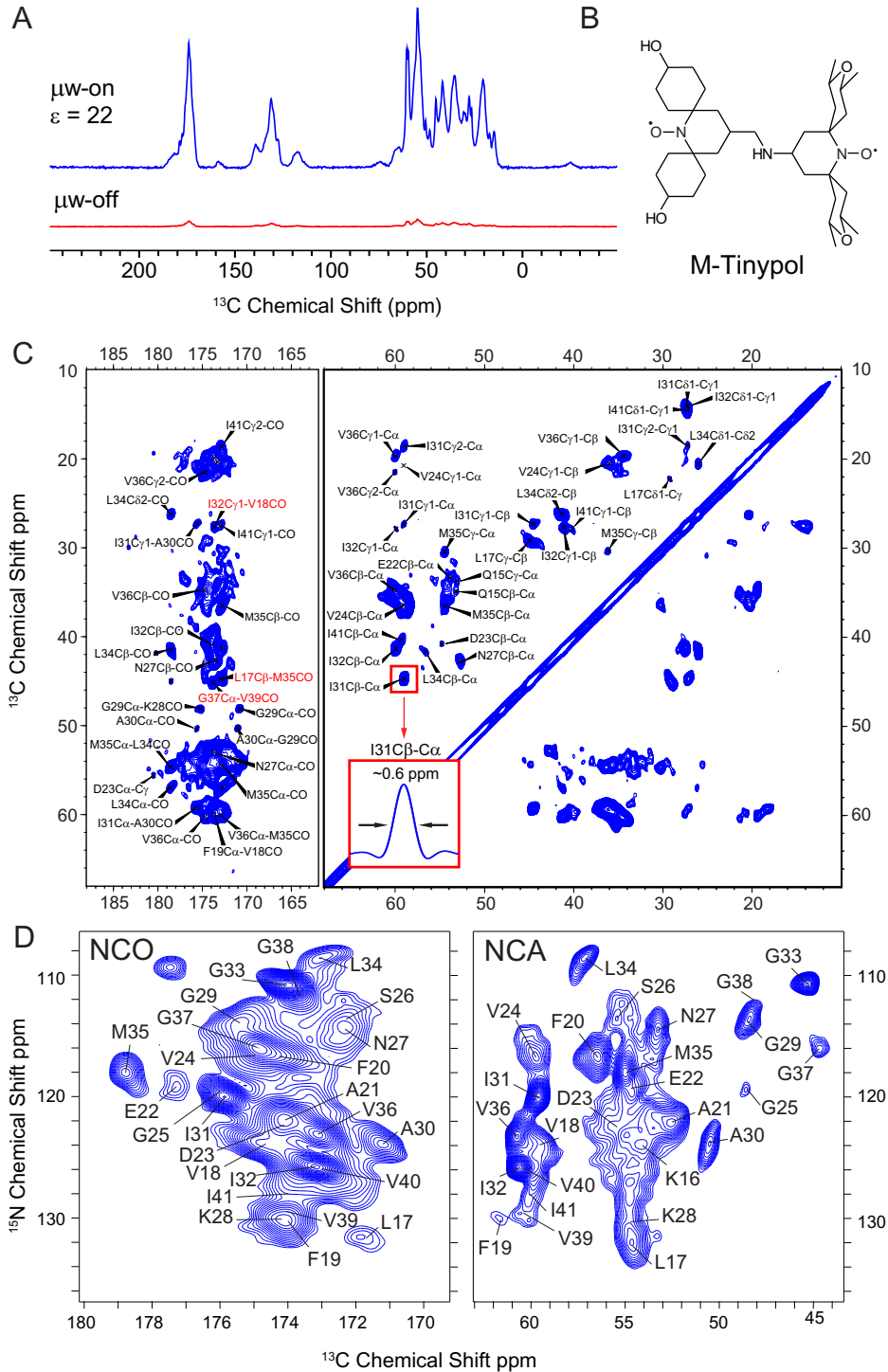
Fig. 3. (A) DNP enhanced ¹³C spectra of 1,3-¹³C₂/2-¹³C/¹⁵N-labeled $M_0A\beta_{1-42}$ illustrating and enhancement of ε = 22 using (B) bis-nitroxide polarizing agent M-TinyPol. (C) DNP-enhanced ¹³C-¹³C CORD-RFDR spectra of 1,3-¹³C₂/2-¹³C/¹⁵N-labeled $M_0A\beta_{1-42}$. The resolution in the spectrum is comparable to that obtained at ambient temperatures, ~0.6 ppm as indicated for I31Cβ-Cα. In red we show the long-range contacts that correspond to the intramolecular monomer structure of the fibril. (D) DNP-enhanced NCO and NCA (Right) spectra acquired using M-TinyPol as the polarizing agent. $\omega_r/2\pi$ = 40 kHz and T = 115 K.

To this end, we combined high-field DNP (800 MHz/527 GHz) with MAS in a 1.3-mm rotor, which permits spinning frequencies up to 40 kHz. In addition, we used a suitably designed water-soluble polarizing agent, M-TinyPol (67), and a selectively labeled 1:1 mixture of 1,3-^{13}C-glycerol/U-^{15}N- and 2-^{13}C-glycerol, U-^{15}N-enriched $M_0A\beta_{1-42}$. Here, the specific labeling scheme offers nearly the full range of labeled spins as that of a uniformly labeled sample but results in considerably sharper linewidths due to the elimination of the J couplings between neighboring ^{13}C nuclei (28, 68–70). The resulting enhancement factor ($\varepsilon = 22$, Fig. 3A) is one of the highest reported to date at this magnetic field on a biomolecular sample and reduces a week's worth of experiment time to approximately one-third of an hour, enabling the rapid acquisition of 2D and 3D MAS NMR experiments with only ~1 mg of sample. Furthermore, this modest enhancement yields a sensitivity ~6.5 times larger than that available from ^{1}H detection at room temperature. Accordingly, improvements in polarizing agents will increase this number. Details of the calculation of this estimate are included in *SI Appendix*.

Importantly, a 2D ^{13}C-^{13}C CORD-RFDR spectrum (Fig. 3C) features resolved cross-peaks from the fibril core with linewidths of ~0.6 ppm, on par with the best results reported for DNP (56, 71–74) and equal to the linewidths we observed in spectra acquired at room temperature. In the carbonyl region, a few long-range contacts that reflect both inter- and intramolecular contacts also appear in the carbonyl region (highlighted in red in Fig. 3C). For example, I32-Cγ1/V18-CO and G37-Cα/V39-CO are consistent with the monomer structure, while L17-Cβ/M35-CO corresponds to the dimer interface. DNP enhanced NCO and NCA spectra (Fig. 3D) also display very good resolution in the ^{15}N dimension and feature all the signals from residues in the 15 to 22 range. Notably, the intensity is lower for residues 22 to 25, corresponding to a loop, which is more dynamical at room temperature. This is consistent with a broader distribution of shifts corresponding to the freezing of multiple conformations. The spectra additionally reveal several peaks that were not present in the equivalent experiment at room temperature (24). These likely arise because cryogenic conditions required by DNP quench any dynamics that would otherwise interfere with the ^{1}H decoupling and thus attenuate peak intensities (75, 76). Concurrently, the microwave enhancement could potentially bring out minor polymorphs as well as the otherwise disordered or dynamic N-terminal region, opening new windows to study the extent of the fibrils' heterogeneity.

The excellent resolution and sensitivity suggest that resolved site-specific contacts could be monitored by combining these 2D datasets in 3D experiments. A pair of 3D NCACX and NCOCX spectra can be acquired by appending a ^{13}C-^{13}C CORD-RFDR mixing to NCO and NCA modules. Fig. 4 shows for the fragment I31-V36 how the joint analysis of these spectra yields both sequential linking of the resonances and contacts between ^{13}CO and ^{13}Cα/^{13}Cβ across the interface of two stacked molecules. On the one hand, this demonstrates the possibility to perform an independent backbone sequential assignment of ^{13}C and ^{15}N resonances directly under cryogenic conditions, extending a strategy proposed by Sergeyev et al. (74). Notably, joint analysis of the NCACX and NCOCX pair allows us to associate each ^{15}N frequency with those of the ^{13}Cαs of both the same and the previous residue. This is illustrated in Fig. 4, where residues I31-I32-G33 and L34-M35-V36 feature a clear sequential connectivity along the backbone. On the other hand, given the mixed labeling, we can easily highlight long-range contacts that reflect intermolecular proximities. For example, among the strips displayed in Fig. 4, we observe CA/CO correlations for G33, L34, and V36, which is consistent with the parallel-in-register architecture. The same strategy also allows us to detect unambiguous correlations such as, e.g., L17-Cβ/M35-CO, corresponding to the dimer interface. Overall, these DNP experiments show that combining high-field, fast-spinning, up-to-date biradical polarizing agents, and specific labeling schemes, produces a wealth of structural information in amyloid fibrils not available in other experiments. These data advantageously complement the capacity of the ^{1}H-detected experiments described earlier.

Conclusions

The possibility of directly recording and assigning resolved resonances throughout the backbone and sidechains is key for obtaining a large set of contacts in amyloid fibrils. Here we have shown that this information can be accessed using only submilligram sample amounts and without the need for deuteration from high-field ^{1}H-detected NMR with 110 kHz MAS and using high-field MAS DNP. Our results demonstrate the significant benefits of these methodologies in the context of amyloid studies and suggest the potential to perform high-throughput analyses of different amyloid constructs without requiring preparation of large quantities of protein or even to study unlabeled peptides derived from tissue samples available in limited quantities.

Additionally, the high-spectral resolution provided by high-spinning frequencies and large signal enhancements reported here lays the groundwork for implementing ^{1}H detection and DNP in a combined fashion for amyloid research in the near future. The ultimate purpose of our exploration is to determine whether combining ^{1}H detection and high-field DNP may be
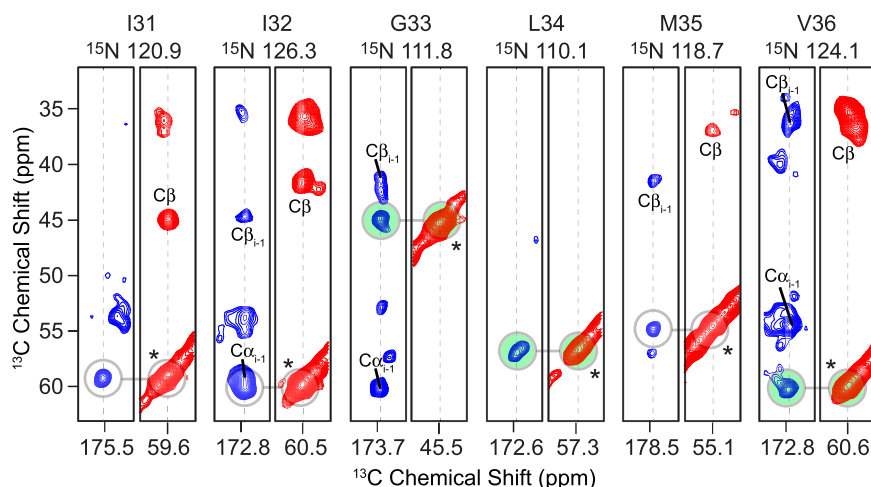
Fig. 4. Selected cross-sections from DNP-enhanced NCOCX (blue) and NCACX (red) spectra of 1,3-$^{13}C_2$/2-^{13}C/^{15}N-labeled M_0-Aβ_{1-42}. Green circles indicate signals that reflect the interdimer contacts and the parallel-in-register arrangement of the fibrils. Asterisks mark diagonal peaks.

feasible for studying fibrils. Together with the ε ~22 enhancement from M-TinyPol, ^{1}H-detected DNP at low temperature may bring a factor of several thousandfold increase in sensitivity, which will likely improve with further development of heterobiradical polarizing agents. Indeed, ^{1}H-detected DNP experiments have recently been accomplished on histidine at 65 kHz MAS and 100 K at high field (77). Extending this work to amyloid fibrils at natural abundance is thus a challenge that is within reach, and these possibilities will enhance our understanding of molecular events underlying Alzheimer's disease and improve the perspectives for therapeutic invention.

Materials and Methods

Sample Preparation. The biosynthetic preparation of U-^{13}C/^{15}N M$_0$Aβ$_{1-42}$ fibril samples was accomplished by expression of the M$_0$Aβ$_{1-42}$ peptide in *Escherichia coli* in M9 minimal medium supplemented with ^{15}N-ammonium chloride and ^{13}C$_6$-glucose and purification of the peptide from inclusion bodies using ion exchange and size exclusion chromatography, followed by a second size exclusion step to isolate pure monomer prior to spontaneous fibril formation under quiescent conditions. This procedure was used previously (24, 28, 35) and is adapted from Walsh et al. (23). The 1,3/2-^{13}C glycerol/^{15}N mixture used in the DNP experiments was prepared by expressing the peptide in *E. coli* in two different M9 media, one containing 1,3-^{13}C$_2$ glycerol and the other with 2-^{13}C glycerol. The peptides were purified independently but then combined as monomers after the final size exclusion step, using the absorbance of the collected monomer peak to determine the concentration of each sample before preparing a 1:1 mixture of the two ^{13}C-labeled variants. Fibrils were formed by incubating the mixture under quiescent conditions, at pH = 8.

^{1}H Detection Experiments. For the ^{1}H-detected experiments, U-^{13}C,^{15}N-M$_0$Aβ$_{1-42}$-labeled fibrils were resuspended in water and directly centrifuged at 165,000 × *g* for 15 h at 12 °C into the NMR rotor using a device provided by Giotto Biotech, similar to those described in the literature (78, 79).

All spectra were acquired at the static field of 23.5 T (1,000 MHz ^{1}H) with a three-channel (HCN) 0.7-mm Bruker MAS probe and at the static field of 18.8 T (800 MHz ^{1}H) with a four-channel (HCND) 0.7-mm Bruker MAS probe. The sample was spun at 111.111 kHz, and we maintained the temperature using a Bruker cooling unit (BCU III) with a regulated dry N$_2$ gas directed at the rotor. The temperature detected by the sensor (260 K) at the point where bearing, drive, and variable temperature gases are mixed, corresponds to roughly 285 ± 5 K inside the 0.7-mm rotor. On both probes, high-power pulse durations were 2.5, 3.5, and 4.5 μs for ^{1}H, ^{13}C, and ^{15}N, respectively. ^{1}H, ^{13}C, and ^{15}N chemical shift data are available in the Biological Magnetic Resonance Data Bank.

The pulse sequences follow, with no modifications, those described in Barbet-Massin et al. (60), Andreas et al. (50) and Stanek et al. (51). For the dipolar-based ^{15}N,^{1}H and ^{13}C,^{1}H CP-HSQC experiments, ^{1}H-^{15}N and ^{1}H-^{13}C CP transfers were optimized around nutation frequencies of 5/4 ω$_r$ and 1/4 ω$_r$, respectively, for proton and ^{15}N (or ^{13}C), with a 10% linear ramp applied on the ^{1}H channel. For 3D CANH and (H)(CO)CA(CO)NH (80), ^{13}C-^{15}N CP was performed with a 10% tangent ramp applied on the ^{15}N frequency at 2/5 ω$_r$, while the ^{13}C nutation frequency was kept around 3/5 ω$_r$. The H(C)CH and (H)CCH

TOCSY sequences were implemented with composite ^{13}C pulses applied with a low nutation frequency of one-fourth the MAS frequency (~27.5 kHz).

In 3D (H)NHH, (H)CHH, and (H)C(H)CH spectra, ^{1}H-^{1}H RFDR recoupling (81–83) was applied after the first back-CP at a ^{1}H RF frequency of 100 kHz, yielding ^{1}H-^{1}H contacts resolved using the shift of ^{15}N or aliphatic ^{13}C.

In all experiments, low power WALTZ-16 decoupling of 10 kHz was employed for heteronuclear decoupling, while ^{13}C decoupling during acquisition was performed with DIPSI-2 irradiation of γB$_1$/2π = 20 kHz. The MISSISSIPPI scheme (84) without the homospoil gradient was used for 100 ms in order to suppress the water signal.

Spectra were apodized in each dimension with 60° shifted squared sine bells ("qsine 3" in Bruker TopSpin), and zero filled to at least twice the number of points in the indirect dimensions. Where linewidths are reported, no apodization was applied for the reported frequency. Acquisition parameters specific for each spectrum can be found in *SI Appendix*, Table S1.

Experimental Parameters for DNP. For the DNP MAS experiments, we resuspended M$_0$Aβ$_{1-42}$ fibrils prepared from a mixture of 1,3-^{13}C-glycerol and 2-^{13}C-glycerol–labeled samples in 25 μL of DNP juice (d$_8$-glycerol/D$_2$O/H$_2$O 60/30/10) containing 10 mM of M-TinyPol. The suspension was left in the refrigerator overnight and packed into a 1.3-mm ZrO$_2$ rotor the following morning by centrifugation for 3 h at 120,000 × *g* and 4 °C.

DNP MAS NMR spectra were recorded on a Bruker Avance III wide bore spectrometer, operating at 18.8 T and equipped with a triple resonance H/X/Y 1.3-mm low-temperature MAS probe. The sample was irradiated with high-power microwaves at a frequency of 527 GHz generated by a gyrotron that was operating continuously during the DNP experiments (stability of better than ±1%). A microwave power of 22 W was used (measured at the bottom of the probe), with a field position we adjusted for optimal cross-effect. The MAS rate was 40 kHz. Sample temperature, estimated from a sensor placed inside the stator that measures the temperature of gas flows around the rotor, was about 115 K (the variable temperature unit was 95.0 K, bearing 94.5 K, drive 127.8 K). High-power pulse durations were 2.5, 3, and 6 μs for ^{1}H, ^{13}C, and ^{15}N, respectively. For all experiments, ^{1}H-^{15}N CP transfers were optimized around nutation frequencies of 100 kHz for proton and 60 kHz for ^{15}N or ^{13}C, with a 50% linear ramp applied on the ^{1}H channel. CP transfers between ^{13}C and ^{15}N were performed with a 10% tangent ramp applied on the ^{15}N frequency at 15 kHz, while the ^{13}C nutation frequency was kept around 25 kHz. The ^{13}C-^{13}C CORD-RFDR experiment was recorded as described by Hou et al. (85), with a mixing time of 104 ms. In the NCOCX and NCACX experiments, we employed the CORD-RFDR mixing scheme for an identical duration.

Spectra were apodized in each dimension with 60° shifted squared sine bells (qsine 3 in Bruker TopSpin) and zero filled to at least twice the number of points in the indirect dimensions. Details about the used acquisition and processing parameters are given in *SI Appendix*, Table S2 below.

Data Availability. All study data are included in the article and/or *SI Appendix*.

1. F. Chiti, C. M. Dobson, Protein misfolding, functional amyloid, and human disease. *Annu. Rev. Biochem.* **75**, 333–366 (2006).

2. D. Eisenberg, M. Jucker, The amyloid state of proteins in human diseases. *Cell* **148**, 1188–1203 (2012).

3. A. S. Cohen, Amyloidosis. *N. Engl. J. Med.* **277**, 522–530 (1967).

4. G. G. Glenner, Amyloid deposits and amyloidosis. The beta-fibrilloses (first of two parts). *N. Engl. J. Med.* **302**, 1283–1292 (1980).

5. G. G. Glenner, C. W. Wong, Alzheimer's disease: Initial report of the purification and characterization of a novel cerebrovascular amyloid protein. *Biochem. Biophys. Res. Commun.* **120**, 885–890 (1984).

6. H. V. Vinters, J. J. Gilbert, Cerebral amyloid angiopathy: Incidence and complications in the aging brain. II. The distribution of amyloid vascular changes. *Stroke* **14**, 924–928 (1983).

7. 2021 Alzheimer's disease facts and figures. *Alzheimers Dement.* **17**, 327–406 (2021).

8. T. Oltersdorf et al., The Alzheimer amyloid precursor protein. Identification of a stable intermediate in the biosynthetic/degradative pathway. *J. Biol. Chem.* **265**, 4492–4497 (1990).

9. D. J. Selkoe, Alzheimer's disease: Genes, proteins, and therapy. *Physiol. Rev.* **81**, 741–766 (2001).

10. G. Brinkmalm et al., Identification of neurotoxic cross-linked amyloid-β dimers in the Alzheimer's brain. *Brain* **142**, 1441–1457 (2019).

11. D. S. Eisenberg, M. R. Sawaya, "Structural studies of amyloid proteins at the molecular level" in *Annual Review of Biochemistry*, R. D. Kornberg, Ed. (Annual Reviews, Palo Alto, 2017), vol. **86**, pp. 69–95.

12. A. W. P. Fitzpatrick et al., Atomic structure and hierarchical assembly of a cross-β amyloid fibril. *Proc. Natl. Acad. Sci. U.S.A.* **110**, 5468–5473 (2013).

13. A. W. P. Fitzpatrick et al., Cryo-EM structures of tau filaments from Alzheimer's disease. *Nature* **547**, 185–190 (2017).

14. U. Ghosh, K. R. Thurber, W.-M. Yau, R. Tycko, Molecular structure of a prevalent amyloid-β fibril polymorph from Alzheimer's disease brain tissue. *Proc. Natl. Acad. Sci. U.S.A.* **118**, e2023089118 (2021).

15. L. Gremer et al., Fibril structure of amyloid-β(1-42) by cryo-electron microscopy. *Science* **358**, 116–119 (2017).

16. M. G. Iadanza et al., The structure of a β$_2$-microglobulin fibril suggests a molecular basis for its amyloid polymorphism. *Nat. Commun.* **9**, 4517 (2018).

17. P. C. Ke et al., Half a century of amyloids: Past, present and future. *Chem. Soc. Rev.* **49**, 5473–5509 (2020).

18. M. Kollmer et al., Cryo-EM structure and polymorphism of Aβ amyloid fibrils purified from Alzheimer's brain tissue. *Nat. Commun.* **10**, 4760 (2019).

19. R. G. S. Spencer et al., An unusual peptide conformation may precipitate amyloid formation in Alzheimer's disease: Application of solid-state NMR to the determination of protein secondary structure. *Biochemistry* **30**, 10382–10387 (1991).

20. P. T. Lansbury et al., Structural model for the b amyloid fibril: Interstrand alignment of an antiparallel b sheet comprising a C-terminal peptide. Nat. Struct. Biol. **2**, 990–997 (1995).

21. A. Loquet et al., 3D structure determination of amyloid fibrils using solid-state NMR spectroscopy. Methods **138-139**, 26–38 (2018).

22. C. P. Jaroniec, Two decades of progress in structural and dynamic studies of amyloids by solid-state NMR. J. Magn. Reson. **306**, 42–47 (2019).

23. D. M. Walsh et al., A facile method for expression and purification of the Alzheimer's disease-associated amyloid beta-peptide. FEBS J. **276**, 1266–1281 (2009).

24. M. T. Colvin et al., High resolution structural characterization of Aβ42 amyloid fibrils by magic angle spinning NMR. J. Am. Chem. Soc. **137**, 7509–7518 (2015).

25. A. T. Petkova, W. M. Yau, R. Tycko, Experimental constraints on quaternary structure in Alzheimer's beta-amyloid fibrils. Biochemistry **45**, 498–512 (2006).

26. J. X. Lu et al., Molecular structure of β-amyloid fibrils in Alzheimer's disease brain tissue. Cell **154**, 1257–1268 (2013).

27. A. K. Schuetz et al., Atomic-resolution three-dimensional structure of amyloid-b fibrils bearing the Osaka mutation. Angew. Chem. Int. Ed. **54**, 331–335 (2015).

28. M. T. Colvin et al., Atomic resolution structure of monomorphic Aβ42 amyloid fibrils. J. Am. Chem. Soc. **138**, 9663–9674 (2016).

29. M. A. Wälti et al., Atomic-resolution structure of a disease-relevant Aβ(1-42) amyloid fibril. Proc. Natl. Acad. Sci. U.S.A. **113**, E4976–E4984 (2016).

30. C. P. Jaroniec et al., High-resolution molecular structure of a peptide in an amyloid fibril determined by magic angle spinning NMR spectroscopy. Proc. Natl. Acad. Sci. U.S.A. **101**, 711–716 (2004).

31. C. Wasmer et al., Amyloid fibrils of the HET-s(218-289) prion form a beta solenoid with a triangular hydrophobic core. Science **319**, 1523–1526 (2008).

32. G. T. Debelouchina et al., Higher order amyloid fibril structure by MAS NMR and DNP spectroscopy. J. Am. Chem. Soc. **135**, 19237–19247 (2013).

33. T. V. Can, R. T. Weber, J. J. Walish, T. M. Swager, R. G. Griffin, Frequency-swept integrated solid effect. Angew. Chem. Int. Ed. Engl. **56**, 6744–6748 (2017).

34. M. D. Tuttle et al., Solid-state NMR structure of a pathogenic fibril of full-length human α-synuclein. Nat. Struct. Mol. Biol. **23**, 409–415 (2016).

35. R. Silvers et al., Aggregation and fibril structure of AβM01-42 and Aβ1-42. Biochemistry **56**, 4850–4859 (2017).

36. M. M. Maricq, J. S. Waugh, NMR in rotating solids. J. Chem. Phys. **70**, 3300–3316 (1979).

37. Y. C. Su, L. Andreas, R. G. Griffin, "Magic angle spinning NMR of proteins: High-frequency dynamic nuclear polarization and H-1 detection" in Annual Review of Biochemistry, R. D. Kornberg, Ed. (Annual Reviews, Palo Alto, 2015), **vol. 84**, pp. 465–497.

38. G. Bodenhausen, D. J. Ruben, Natural abundance N-15 NMR by enhanced heteronuclear spectroscopy. Chem. Phys. Lett. **69**, 185–189 (1980).

39. R. R. Ernst, G. Bodenhausen, A. Wokaun, Principles of Nuclear Magnetic Resonance in One and Two Dimensions (Clarendon Press, Oxford, 1991), **vol. 14**.

40. Y. Ishii, R. Tycko, Sensitivity enhancement in solid state (15)N NMR by indirect detection with high-speed magic angle spinning. J. Magn. Reson. **142**, 199–204 (2000).

41. T. Maly et al., Dynamic nuclear polarization at high magnetic fields. J. Chem. Phys. **128**, 052211 (2008).

42. Q. Z. Ni et al., High frequency dynamic nuclear polarization. Acc. Chem. Res. **46**, 1933–1941 (2013).

43. A. B. Barnes et al., High-field dynamic nuclear polarization for solid and solution biological NMR. Appl. Magn. Reson. **34**, 237–263 (2008).

44. A. S. Lilly Thankamony, J. J. Wittmann, M. Kaushik, B. Corzilius, Dynamic nuclear polarization for sensitivity enhancement in modern solid-state NMR. Prog. Nucl. Magn. Reson. Spectrosc. **102-103**, 120–195 (2017).

45. A. B. Barnes et al., Cryogenic sample exchange NMR probe for magic angle spinning dynamic nuclear polarization. J. Magn. Reson. **198**, 261–270 (2009).

46. R. Linser et al., Proton-detected solid-state NMR spectroscopy of fibrillar and membrane proteins. Angew. Chem. Int. Ed. Engl. **50**, 4508–4512 (2011).

47. A. A. Smith et al., Partially-deuterated samples of HET-s(218-289) fibrils: Assignment and deuterium isotope effect. J. Biomol. NMR **67**, 109–119 (2017).

48. T. Le Marchand et al., Conformational dynamics in crystals reveal the molecular bases for D76N beta-2 microglobulin aggregation propensity. Nat. Commun. **9**, 1658 (2018).

49. S. Asami, B. Reif, Accessing methyl groups in proteins via ¹H-detected MAS solid-state NMR spectroscopy employing random protonation. Sci. Rep. **9**, 15903 (2019).

50. L. B. Andreas et al., Structure of fully protonated proteins by proton-detected magic angle spinning NMR. Proc. Natl. Acad. Sci. **113**, 9187–9192 (2016).

51. J. Stanek et al., NMR spectroscopic assignment of backbone and side-chain protons in fully protonated proteins: Microcrystals, sedimented assemblies, and amyloid fibrils. Angew. Chem. Int. Ed. Engl. **55**, 15504–15509 (2016).

52. A. Daskalov et al., Structural and molecular basis of cross-seeding barriers in amyloids. Proc. Natl. Acad. Sci. U.S.A. **118**, 8 (2021).

53. G. T. Debelouchina et al., Dynamic nuclear polarization-enhanced solid-state NMR spectroscopy of GNNQQNY nanocrystals and amyloid fibrils. Phys. Chem. Chem. Phys. **12**, 5911–5919 (2010).

54. J. M. Lopez del Amo, D. Schneider, A. Loquet, A. Lange, B. Reif, Cryogenic solid state NMR studies of fibrils of the Alzheimer's disease amyloid-β peptide: Perspectives for DNP. J. Biomol. NMR **56**, 359–363 (2013).

55. P. Fricke et al., High resolution observed in 800 MHz DNP spectra of extremely rigid type III secretion needles. J. Biomol. NMR **65**, 121–126 (2016).

56. Q. Z. Ni et al., Primary transfer step in the light-driven ion pump bacteriorhodopsin: An irreversible U-turn revealed by dynamic nuclear polarization-enhanced magic angle spinning NMR. J. Am. Chem. Soc. **140**, 4085–4091 (2018).

57. K. Jaudzems et al., Dynamic nuclear polarization-enhanced biomolecular NMR spectroscopy at high magnetic field with fast magic-angle spinning. Angew. Chem. Int. Ed. Engl. **57**, 7458–7462 (2018).

58. A. Wickramasinghe et al., Sensitivity-enhanced solid-state NMR detection of structural differences and unique polymorphs in pico- to nanomolar amounts of brain-derived and synthetic 42-residue amyloid-β fibrils. J. Am. Chem. Soc. **143**, 11462–11472 (2021).

59. E. K. Paulson et al., Sensitive high resolution inverse detection NMR spectroscopy of proteins in the solid state. J. Am. Chem. Soc. **125**, 15831–15836 (2003).

60. E. Barbet-Massin et al., Rapid proton-detected NMR assignment for proteins with fast magic angle spinning. J. Am. Chem. Soc. **136**, 12489–12497 (2014).

61. C. Lendel et al., Combined solution- and magic angle spinning NMR reveals regions of distinct dynamics in amyloid beta protofibrils. ChemistrySelect **1**, 5850–5853 (2016).

62. V. Agarwal et al., De novo 3D structure determination from sub-milligram protein samples by solid-state 100 kHz MAS NMR spectroscopy. Angew. Chem. Int. Ed. Engl. **53**, 12253–12256 (2014).

63. J. S. Retel et al., Structure of outer membrane protein G in lipid bilayers. Nat. Commun. **8**, 2073 (2017).

64. T. Schubeis et al., A β-barrel for oil transport through lipid membranes: Dynamic NMR structures of AlkL. Proc. Natl. Acad. Sci. U.S.A. **117**, 21014–21021 (2020).

65. G. T. Debelouchina, G. W. Platt, M. J. Bayro, S. E. Radford, R. G. Griffin, Intermolecular alignment in β2-microglobulin amyloid fibrils. J. Am. Chem. Soc. **132**, 17077–17079 (2010).

66. M. J. Bayro et al., Intermolecular structure determination of amyloid fibrils with magic-angle spinning and dynamic nuclear polarization NMR. J. Am. Chem. Soc. **133**, 13967–13974 (2011).

67. A. Lund et al., TinyPols: A family of water-soluble binitroxides tailored for dynamic nuclear polarization enhanced NMR spectroscopy at 18.8 and 21.1 T. Chem. Sci. (Camb.) **11**, 2810–2818 (2020).

68. D. M. LeMaster, D. M. Kushlan, Dynamical mapping of E. coli thioredoxin via ¹³C NMR relaxation analysis. J. Am. Chem. Soc. **118**, 9255–9264 (1996).

69. J. Pauli, B. van Rossum, H. Förster, H. J. de Groot, H. Oschkinat, Sample optimization and identification of signal patterns of amino acid side chains in 2D RFDR spectra of the alpha-spectrin SH3 domain. J. Magn. Reson. **143**, 411–416 (2000).

70. M. Hong, Determination of multiple φ-torsion angles in proteins by selective and extensive (13)C labeling and two-dimensional solid-state NMR. J. Magn. Reson. **139**, 389–401 (1999).

71. V. S. Bajaj, M. L. Mak-Jurkauskas, M. Belenky, J. Herzfeld, R. G. Griffin, DNP enhanced frequency-selective TEDOR experiments in bacteriorhodopsin. J. Magn. Reson. **202**, 9–13 (2010).

72. P. Fricke, J. P. Demers, S. Becker, A. Lange, Studies on the MxiH protein in T3SS needles using DNP-enhanced ssNMR spectroscopy. ChemPhysChem **15**, 57–60 (2014).

73. X. Lu, C. Guo, G. Hou, T. Polenova, Combined zero-quantum and spin-diffusion mixing for efficient homonuclear correlation spectroscopy under fast MAS: Broadband recoupling and detection of long-range correlations. J. Biomol. NMR **61**, 7–20 (2015).

74. I. V. Sergeyev, B. Itin, R. Rogawski, L. A. Day, A. E. McDermott, Efficient assignment and NMR analysis of an intact virus using sequential side-chain correlations and DNP sensitization. Proc. Natl. Acad. Sci. U.S.A. **114**, 5171–5176 (2017).

75. J. R. Long, B. Q. Sun, A. Bowen, R. G. Griffin, Molecular-dynamics and magic-angle-spinning Nmr. J. Am. Chem. Soc. **116**, 11950–11956 (1994).

76. Q. Z. Ni et al., Peptide and protein dynamics and low-temperature/DNP magic angle spinning NMR. J. Phys. Chem. B **121**, 4997–5006 (2017).

77. P. Berruyer et al., Dynamic nuclear polarization enhancement of 200 at 21.15 T enabled by 65 kHz magic angle spinning. J. Phys. Chem. Lett. **11**, 8386–8391 (2020).

78. A. Böckmann et al., Characterization of different water pools in solid-state NMR protein samples. J. Biomol. NMR **45**, 319–327 (2009).

79. I. Bertini et al., Solid-state NMR of proteins sedimented by ultracentrifugation. Proc. Natl. Acad. Sci. U.S.A. **108**, 10396–10399 (2011).

80. E. Barbet-Massin et al., Out-and-back 13C-13C scalar transfers in protein resonance assignment by proton-detected solid-state NMR under ultra-fast MAS. J. Biomol. NMR **56**, 379–386 (2013).

81. A. E. Bennett, J. H. Ok, R. G. Griffin, S. Vega, Chemical-shift correlation spectroscopy in rotating solids – Radio frequency-driven dipolar recoupling and longitudinal exchange. J. Chem. Phys. **96**, 8624–8627 (1992).

82. A. E. Bennett et al., Homonuclear radio frequency-driven recoupling in rotating solids. J. Chem. Phys. **108**, 9463–9479 (1998).

83. M. J. Bayro, R. Ramachandran, M. A. Caporini, M. T. Eddy, R. G. Griffin, Radio frequency-driven recoupling at high magic-angle spinning frequencies: Homonuclear recoupling sans heteronuclear decoupling. J. Chem. Phys. **128**, 052321 (2008).

84. D. H. Zhou, C. M. Rienstra, High-performance solvent suppression for proton detected solid-state NMR. J. Magn. Reson. **192**, 167–172 (2008).

85. G. Hou, S. Yan, J. Trébosc, J. P. Amoureux, T. Polenova, Broadband homonuclear correlation spectroscopy driven by combined R2(n)(v) sequences under fast magic angle spinning for NMR structural analysis of organic and biological solids. J. Magn. Reson. **232**, 18–30 (2013).